NANO · MICRO small
www.small-journal.com

Atomically Thin $TaSe_2$ Film as a High-Performance Substrate for Surface-Enhanced Raman Scattering

Yuancai Ge, Fei Wang, Ying Yang, Yi Xu, Ying Ye, Yu Cai, Qingwen Zhang, Shengying Cai, DanFeng Jiang, Xiaohu Liu, Bo Liedberg, Jian Mao, and Yi Wang**

An atomically thin $TaSe_2$ sample, approximately containing two to three layers of $TaSe_2$ nanosheets with a diameter of 2.5 cm is prepared here for the first time and applied on the detection of various Raman-active molecules. It achieves a limit of detection of 10^{-10} M for rhodamine 6G molecules. The excellent surface-enhanced Raman scattering (SERS) performance and underlying mechanism of $TaSe_2$ are revealed using spectrum analysis and density functional theory. The large adsorption energy and the abundance of filled electrons close to the Fermi level are found to play important roles in the chemical enhancement mechanism. Moreover, the $TaSe_2$ film enables highly sensitive detection of bilirubin in serum and urine samples, highlighting the potential of using 2D SERS substrates for applications in clinical diagnosis, for example, in the diagnosis of jaundice caused by excess bilirubin in newborn children.

1. Introduction

Surface-enhanced Raman spectroscopy is an efficient and sensitive method that is used for the nondestructive detection of various molecules. It has received extensive attention in the fields of analytical chemistry,[1] environmental science,[2] and biomedical engineering.[3] Since the discovery of the surface-enhanced Raman scattering (SERS) effect close to a silver electrode around 1970,[4] numerous efforts have been made to develop SERS substrates, including the fabrication of noble metal nanoparticles and well-prepared nanostructures.[5,6] The conventional SERS effect mainly arises from electromagnetic (EM) enhancement, as the plasmon resonance close to the rough metallic surface or the metal nanoparticles enables enhanced excitation.[7] In recent decades, noble metals, such as gold and silver, with a resonance frequency containing the range of visible light, have been widely studied owing to their significant enhancement factors (EF).[8] It is generally accepted that the SERS signals are mainly derived from ultrahigh localized electric fields, named hot spots. In some cases, a surface in which only a small proportion of the probes is close to the hot spots (<1% of the total surface) can contribute more than 80% of the total SERS signals.[9] However, SERS techniques relying on EM enhancement require the use of delicate, precisely fabricated and costly noble metal nanostructures to achieve reproducible, reliable, and sensitive analysis.

In addition, chemical mechanism (CM) offers another important SERS mechanism relying on charge transfer (CT) between the analytes and substrates. Furthermore, the most studied semiconductors, such as ZnO and TiO_2, are cheaper than gold and silver nanostructures and easier to fabricate.[10,11] However, the SERS performance of these semiconductors and other highly doped semiconductors are not comparable to those of noble metals owing to their low charge carrier density. Recently reported 2D materials, including graphene, MoS_2, WS_2, h-BN, and ReS_2,[12–14] are the most commonly reported SERS substrates with CT resonances. However, the limited factor is the population of electrons at states close to the Fermi level. It hampers the CT efficiency of these 2D materials, and a significant amount of research has been devoted to strategies to increase the density of state (DOS) close to the Fermi level to improve their SERS performance. According to Fermi's golden rule, the electron transition probability plays an important role in the CT process and it is linearly dependent on the DOS close to the Fermi level.[15] As a result, several strategies, including shifting the Fermi level by doping graphene with nitrogen atoms,[16] changing the phase transition from the semiconductor 2H phase to the metallic 1T phase of MoS_2,[17]

Y. C. Ge, Y. Yang, Y. Ye, Y. Cai, X. H. Liu, Y. Wang
School of Biomedical Engineering
School of Ophthalmology and Optometry
Wenzhou Medical University
Xueyuan Road 270, Wenzhou 325027, China
E-mail: wangyi@wiucas.ac.cn

F. Wang, J. Mao
College of Materials Science and Engineering
Sichuan University
Chengdu 610065, China
E-mail: maojian@scu.edu.cn

Y. Xu
State Key Laboratory for Artificial Microstructures and Mesoscopic Physics
School of Physics
Peking University
Beijing 100871, China

Q. W. Zhang, S. Y. Cai, D. F. Jiang, Y. Wang
Wenzhou Institute
University of Chinese Academy of Sciences
Xinsan Road 16, Wenzhou 325001, China

B. Liedberg
Centre for Biomimetic Sensor Science
School of Materials Science and Engineering
Nanyang Technological University
50 Nanyang Avenue, Singapore 639798, Singapore

The ORCID identification number(s) for the author(s) of this article can be found under https://doi.org/10.1002/smll.202107027.

DOI: 10.1002/smll.202107027

and the introduction of selenium vacancies in WSe_2,[18] have been employed to significantly improve the SERS performance. However, their SERS performance is still not comparable with those of noble metals.

Recently, semimetallic 2D materials with zero bandgap were reported to be ideal candidates for use as SERS substrates owing to their high DOS close to the Fermi level, their atomically flat surface and their strong interaction with the analytes.[19,20] NbS_2 and $NbSe_2$ fabricated using chemical vapor deposition (CVD) yielded an ultralow limit of detection (LOD) for SERS measurements.[15,21] The lateral dimensions of the NbS_2 and $NbSe_2$ nanosheets fabricated using CVD were ≈1–200 µm. The small size of the nanosheets barely meets the requirements of large-scale applications. Other methods, such as liquid exfoliation and mechanical exfoliation, are also inefficient for practical usage.[19,22] As a typical semimetallic 2D material, $TaSe_2$ exhibits a charge density wave (CDW),[23] superconductivity,[24] and tunable electronic structures.[25] Therefore, it may be a suitable candidate for SERS substrate and may offer good performance on Raman biosensors.

Herein, the intercalation of lithium ions into bulk $TaSe_2$ followed by sonication in a water bath was utilized to fabricate $TaSe_2$ nanosheets with a high yield. An atomically thin $TaSe_2$ film with a diameter of 2.5 cm (containing two to three layers of $TaSe_2$ nanosheets) was prepared by filtering the $TaSe_2$ solution through a porous anodic aluminum oxide (AAO) substrate. Results obtained from experiments and density functional theory (DFT) calculations reveal a strong interaction between the $TaSe_2$ nanosheets and the Raman probes. In addition, the higher Fermi level of $TaSe_2$ can expedite the migration of electrons close to the Fermi level to the highest occupied molecular orbital (HOMO) of the SERS probes resulting in a high electron transfer probability.[26] It further demonstrates excellent SERS performance with an LOD of 0.1×10^{-9} M for the detection of rhodamine 6G (R6G) molecules. Moreover, the atomically thin $TaSe_2$ film can be used to detect bilirubin molecules in serum and urine samples to conveniently diagnose jaundice resulting from high levels of bilirubin with an excellent sensitivity.

2. Results and Discussion

2.1. Exfoliation and Characterizations of $TaSe_2$

To obtain atomically thin $TaSe_2$ nanosheets (**Figure 1**a), bulk $TaSe_2$ was reacted with *n*-butyllithium for ≈3 d to form the intermediate precursor (Li_XTaSe_2). Upon sonication of the precursor in water, the resulting hydrogen gas boosts the expansion of the interlayer distance and weakens the van der Waals interactions between adjacent layers of $TaSe_2$. Previous reports have also confirmed the efficient synthesis of high quality 2D transition metal dichalcogenides (TMDs) using lithium intercalation and exfoliation.[27,28] As depicted in Figure 1b, the powder X-ray diffraction (PXRD) patterns of the bulk $TaSe_2$ can be assigned to the 2H phase of $TaSe_2$ using the Joint Committee on Powder Diffraction Standards (JCPDS) No. 19-13030 (pink bars). After exfoliation and deposition of the $TaSe_2$ nanosheets on a silicon wafer chip, the high *c*-axis orientation of the $TaSe_2$ nanosheets was verified using the PXRD patterns (red curve) shown in Figure 1b, in which the diffraction peaks of the (002) facet can be easily observed, along with other diminished peaks.[29] The upshift of the peak at 13.8° indicates the expanded space along the (002) facet direction after exfoliation, and the splitting of this peak denotes the partial 2H phase $TaSe_2$ transforms into 1T phase. The ratio of 2H to 1T is calculated to be about 4:1 with current process of fabrication. The successful exfoliation of $TaSe_2$ was also verified using the Raman spectra, as shown in Figure S1 in the Supporting Information, as two distinct peaks can be observed at around 207 and 234 cm^{-1} that are characteristic for bulk $TaSe_2$.[30,31] The peak at 207 cm^{-1} (E_{2g} mode) is attributed to the vibrational modes of the Ta and Se atoms oscillating in the antiphase, that are parallel to the layer. Furthermore, the peak centered at 234 cm^{-1} (A_{1g} mode) is ascribed to the vibration of the Se atoms in the antiphase mode with fixed Ta atoms that is perpendicular to the layer.[32,33] After exfoliation in water, the E_{2g} (207 cm^{-1}) mode in the bulk $TaSe_2$ noticeably shifts to a higher wavelength of 213 cm^{-1} in the $TaSe_2$ nanosheets, but no obvious shift in the A_{1g} (234 cm^{-1}) is observed.[33] Some of the previous studies based on intercalated $TaSe_2$ and WS_2 have reported that this results from the considerable enhancement of the dielectric screening effect by the long-range Coulomb interaction. Upon increasing the number of layers, the overall restoring force on the atoms is reduced.[31,34] The scanning electron microscopy (SEM) image of the atomically thin $TaSe_2$ nanosheets on the porous AAO substrate shows the lateral size of the prepared $TaSe_2$ nanosheets ranges from 100 nm to 3 µm (Figure 1c). The SERS substrate, with a diameter of 2.5 cm, was prepared by filtering a dispersion of $TaSe_2$ nanosheets through an AAO substrate to obtain an ultrathin AAO covered $TaSe_2$ film (Figure S2, Supporting Information). Figure 1d shows the obtained $TaSe_2$ film close to the edge of the AAO, with an average of two to three layers of $TaSe_2$ nanosheets on the surface of the AAO according to the calculation in Figure S3 in the Supporting Information.

The transmission electron microscopy (TEM) image and element mapping performed using high-angle annular dark-field scanning transmission electron microscopy shown in **Figure 2**a display the homogeneous dispersion of the Ta and Se elements over the $TaSe_2$ nanosheets. The thickness of the $TaSe_2$ nanosheets was measured and observed to be ≈1.6 nm using atomic force microscopy (AFM) in the tapping mode (Figure 2b), which was slightly larger than the thickness of two layers of $TaSe_2$. The crystal axis of the 2H phase $TaSe_2$ along the *z*-direction is ≈1.27 nm (the distance of the (002) facet stated in JCPDS No. 19-13030) and the unit cell contains two layers of $TaSe_2$.[31] The partial phase transition from 2H to 1T is observed in many TMDs owing to the lithiation process.[35–37] Moreover, the high-resolution TEM (HRTEM) image shows the coexistence of the 2H and 1T phases with some disorder close to the phase boundary, as observed in Figure S4 in the Supporting Information. Selected areas have been amplified in Figure S4 in the Supporting Information to demonstrate the typical 2H phase (Figure 2c) and the 1T phase of $TaSe_2$ (Figure 2d). The hexagonal lattice, with bright Ta and dim Se, can be easily distinguished owing to their different atomic numbers. The lattice fringe distance of 2.97 Å is attributed to the (101) facet of the 2H phase $TaSe_2$ and the Ta atom has a trigonal prismatic coordination (Figure 2e).[38] For the 1T phase of $TaSe_2$, the lattice fringe

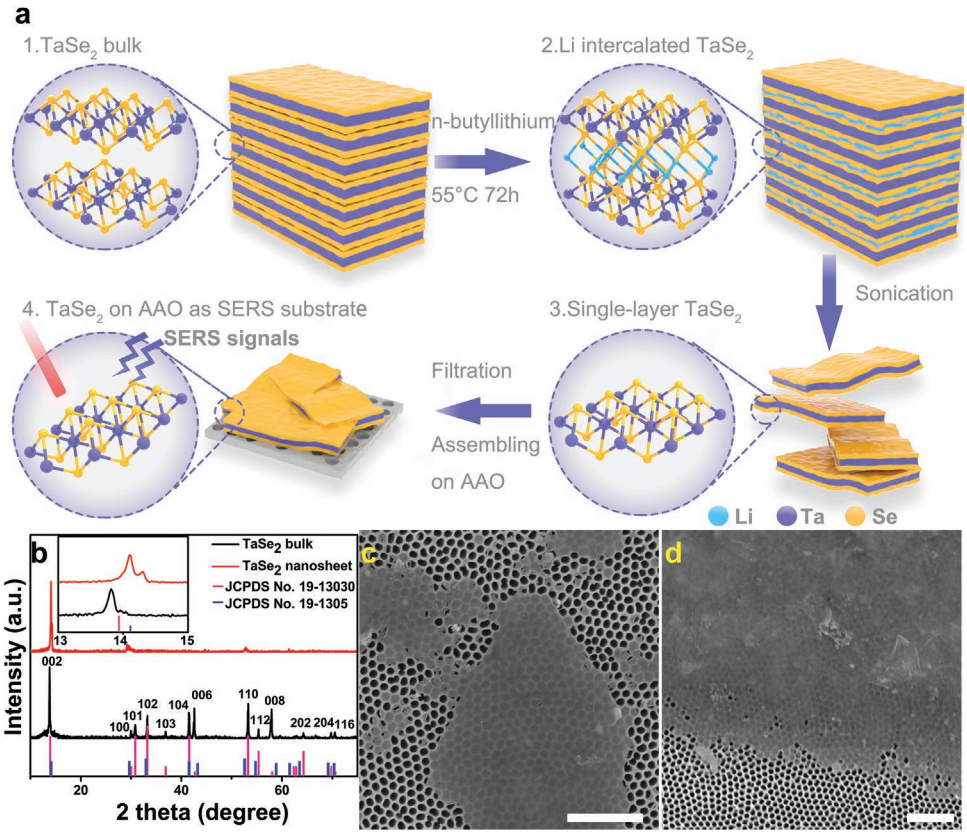

Figure 1. a) Schematic illustration of the fabrication process of the $TaSe_2$ nanosheets. Anhydrous *n*-hexane and 2.5 M *n*-butyllithium were used in a Schlenk line with an argon atmosphere. b) PXRD patterns of the pristine $TaSe_2$ powder (black curve), $TaSe_2$ nanosheets (red curve), and the standard JCPDS data with the pink bars and the blue bars representing the 2H and 1T $TaSe_2$ phases, respectively. c) The SEM image of the $TaSe_2$ nanosheets on the AAO substrate. d) Assembled $TaSe_2$ film on an AAO substrate. The scale bar represents 1 μm.

distance of 2.72 Å can be indexed to the (101) plane (Figure 2d), showing the octahedral coordination of the Ta atom (Figure 2e). The splitting of the two spots from the 2H phase to 1T phase of $TaSe_2$ can be observed from the result of the selected area electron diffraction (Figure S4, Supporting Information), indicating the coexistence of 2H and 1T phases in $TaSe_2$. The coexistence of the 2H and 1T phases in the $TaSe_2$ nanosheets was further verified using X-ray photoelectron spectroscopy (XPS) measurements (Figure S5a, Supporting Information). According to previous reports, the splitting of the peaks centered at 23.3 eV (Ta $4f_{7/2}$) and 25.5 eV (Ta $4f_{5/2}$) shows the typical characteristics of nearly commensurate CDW, which occurs in the 1T $TaSe_2$ phase at room temperature and in the 2H phase at a high temperature.[39,40] Compared with the XPS spectra of the 2H and 1T phase $TaSe_2$,[40] the $TaSe_2$ nanosheets prepared in this work exhibit a reduced split at room temperature, indicating that both the 2H and 1T phases exist in the $TaSe_2$ nanosheets. The core level spectrum illustrated in Figure S5b in the Supporting Information depicts the Se $3d_{5/2}$ (54.5 eV) and $3d_{1/2}$ (53.7 eV) of $TaSe_2$, which is in accordance with previously reported results.[39]

2.2. SERS Performances of $TaSe_2$

To investigate the SERS performance of the $TaSe_2$ film, a typical dye molecule, R6G, was used as a Raman probe. A laser, at a wavelength of 532 nm with a power of 5 mW, was used to investigate the Raman signal of the R6G molecules. **Figure 3**a shows the SERS spectra of the $TaSe_2$ films covered with R6G molecules at different concentrations ranging from 10^{-10} to 10^{-5} M. The conspicuous Raman signals centered at 611, 773, 1182, 1302, 1360, 1501, 1573, and 1650 cm^{-1} are attributed to the different vibrational modes of R6G as listed in Table S1 in the Supporting Information, which are in accordance with previously reported results.[41,42] Interestingly, the Raman signals for the R6G molecules on the $TaSe_2$ film can still be detected at concentrations as low as 10^{-10} M, which is comparable to the sensitivity observed for noble metals, such as gold and silver.[43–45] A comparison of the SERS performance of the $TaSe_2$ film in this study and other TMDs is listed in Table S2 in the Supporting Information. Considering the $TaSe_2$ film was supported on a porous AAO substrate, a control experiment was performed on a bare AAO substrate covered with 10^{-3} M R6G molecules and weak Raman signals were observed for R6G (as shown in Figure 3a), indicating the negligible Raman enhancement from AAO substrate. Due to the low background Raman noise from AAO itself, there is no remarkable Raman interference upon detecting analytes on top of it. The reproducibility of the SERS performance was investigated using 10^{-7} M R6G solution on the $TaSe_2$ film, as depicted in Figure 3b. The SERS mapping depicted from the Raman intensity at 611 cm^{-1} shows a clear boundary and a remarkable contrast in the

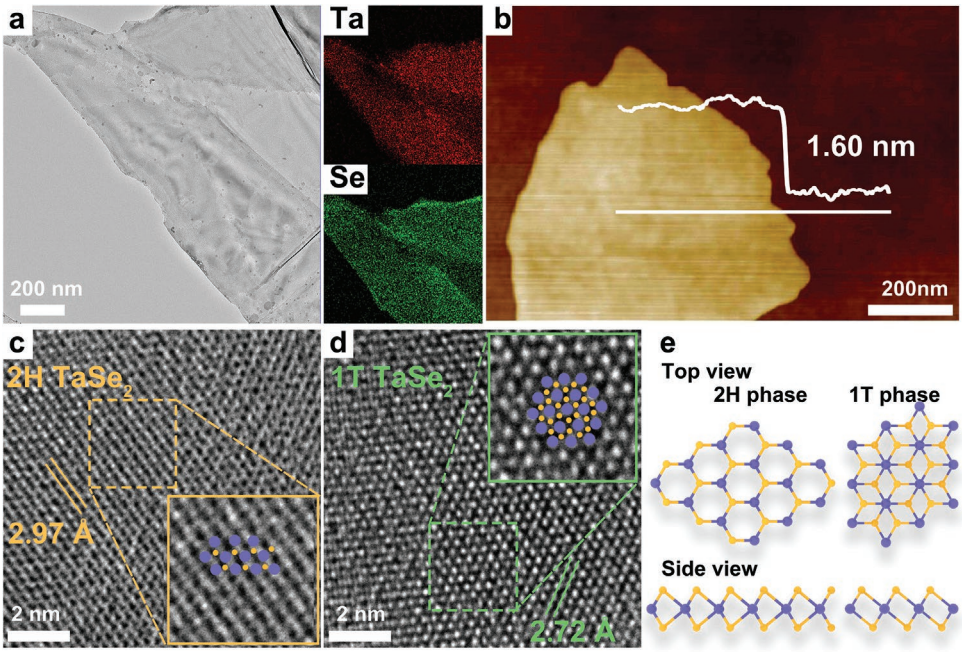

Figure 2. a) TEM image and the corresponding elemental mapping results for the $TaSe_2$ nanosheets. b) AFM image of the $TaSe_2$ nanosheets. HRTEM morphology of the $TaSe_2$ nanosheets with the ordered c) 2H phase and d) 1T phase (bright field images). e) 3D models of the 2H and 1T $TaSe_2$ single layer.

intensity between the $TaSe_2$ film and the bare AAO substrate (Figure 3b). The results indicate a strong Raman EF of 1.5×10^5 is observed upon coating the $TaSe_2$ film. To verify the homogeneity of the SERS signals with the $TaSe_2$ film, 250 Raman

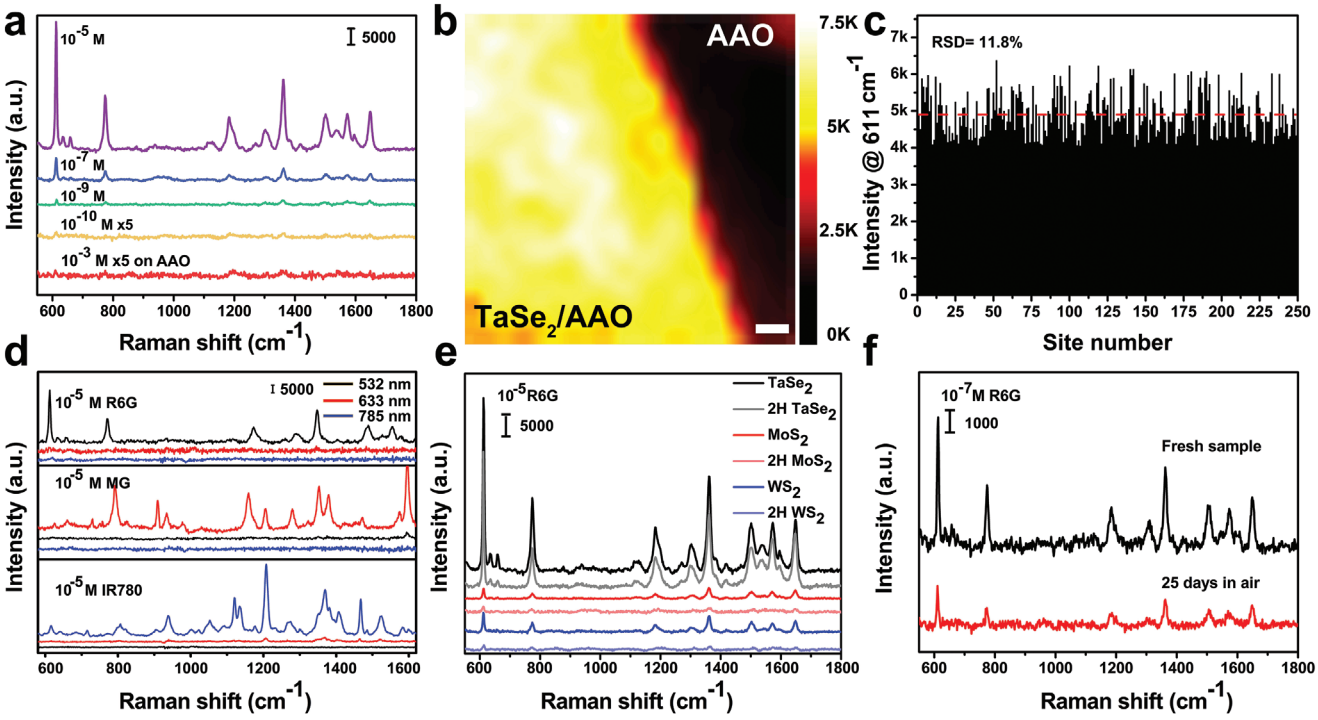

Figure 3. a) SERS signals for the R6G molecules at different concentrations from 10^{-5} to 10^{-10} M. b) SERS mapping of 10^{-7} M R6G close to the edge of the $TaSe_2$ assembled on AAO. The scale bar represents 2 μm. c) The signal variation of 10^{-7} M R6G at the Raman shift of 611 cm^{-1}. d) SERS signals of 10^{-5} M R6G, MG, and IR780 adsorbed on the $TaSe_2$ nanosheets measured using the laser at wavelengths of 532, 633, and 785 nm. e) Comparison of the SERS performance of $TaSe_2$ with the MoS_2 and WS_2 and the pure 2H phase of $TaSe_2$, MoS_2, and WS_2. f) Raman spectra of 10^{-7} M R6G absorbed on the freshly prepared $TaSe_2$ film and a film that has been stored in air for 25 d.

signal points were measured at 611 cm^{-1} and show a relative standard deviation of 11.8% (Figure 3c), indicating the good homogeneity of the prepared film. The universal SERS performance of the $TaSe_2$ film was investigated for different Raman probes, including R6G, Malachite Green (MG) and the IR780 molecules, as shown in Figure 3d. The SERS intensity of the different Raman molecules is strongly dependent on the excitation wavelengths of the laser. The strongest SERS signals for the R6G, MG and IR780 molecules are obtained for excitation at 532, 633, and 785 nm, respectively. The vibrational modes and the corresponding Raman shifts of the MG molecules and the IR780 molecules are also listed in Table S1 in the Supporting Information.[46–50] The SERS signals for the R6G, MG, and IR780 molecules excited at other wavelengths are very weak or cannot be detected at all. This result strongly suggests that the molecular resonance combined with the photons may play the most important role in the SERS mechanism of the $TaSe_2$ film and the photon-induced charge transfer (PICT) is verified in the following discussion. The SERS performance of $TaSe_2$ was also compared with the most frequently studied TMDs, such as MoS_2 and WS_2, prepared via lithium intercalation and liquid-phase exfoliation with ethanol (Figure S6 in the Supporting Information). The lithium intercalated MoS_2 and WS_2 substrates comprise the metallic 1T phase and semiconductive 2H phase. However, the liquid-phase exfoliated MoS_2 and WS_2 samples display only the 2H phase. Figure 3e illustrates that the lithium intercalated MoS_2 and WS_2 show a better performance than the liquid-phase exfoliated 2H phase MoS_2 and WS_2. However, the $TaSe_2$ film provides the highest Raman enhancement among these TMDs (about ten times higher than MoS_2 and WS_2 samples listed in Table S3, Supporting Information). The SERS performance of the pure 2H $TaSe_2$ prepared via liquid phase exfoliation is about 78% of the $TaSe_2$ nanosheets prepared with lithium intercalation (Figure 3e), indicating the process of lithium intercalation is more feasible to produce $TaSe_2$ nanosheets with higher SERS activity. The stability of the $TaSe_2$ film was investigated (Figure 3f) by measuring the 10^{-7} M R6G solution before and after storage in air for 25 d. The SERS signals still show 30.5% of the original intensity at 611 cm^{-1} after 25 d of storage. The stability of $TaSe_2$ film is comparable with other previously reported TMDs film such as $NbSe_2$ fabricated via CVD.[21] The decrease in the SERS intensity is mainly attributed to the partial oxidation of the $TaSe_2$ surface owing to its large surface area, which can be observed in Figure S1 in the Supporting Information. In addition to the E_{2G} and A_{1g} vibrational modes of $TaSe_2$, a peak centered at 260 cm^{-1} appears after 25 d of storage, which is ascribed to surface oxidation of $TaSe_2$.[51]

2.3. SERS Mechanism of $TaSe_2$

To reveal the underlying SERS mechanism of the $TaSe_2$ film, comprehensive spectroscopic analysis and DFT calculations were conducted. The absorption spectra of R6G, MG, and IR780 show their absorption peaks at 530, 620, and 775 nm, respectively (as shown in **Figure 4**a). The dispersion of $TaSe_2$ nanosheets only exhibits a broad absorption peak around 425 nm, which is ascribed to the interband transition of the electrons from the p orbital of the Se atoms to the d orbital of the Ta atoms.[52] After mixing the Raman probes with $TaSe_2$ nanosheets, the absorption peaks for R6G, MG, and IR780 redshift to 553, 643, and 812 nm, respectively, which indicates that their HOMO–lowest unoccupied molecular orbital (LUMO) gaps are narrowed and a more efficient charge transition probability can be achieved.[53] Furthermore, the Raman probes exhibit distinct color changes after mixing with the $TaSe_2$ nanosheets (Figure 4a,b). The absorption spectra show a redshift of the absorption peak for the three Raman probes upon mixing with the $TaSe_2$ nanosheet, owing to the charge transfer between the probes and the $TaSe_2$ nanosheet. It should be noted that the absorption spectra of the mixed solution do not simply overlay the two spectra of the probes and the $TaSe_2$ nanosheet. According to Fermi's golden rule, the electron transition probability can be described as $\omega_{lk} = \frac{2\pi}{\hbar} g(E_k) |H'_{kl}|^2$, in which $\hbar$ is the reduced Planck constant, $g(E_k)$ is the DOS, and H'_{kl} is the matrix element from the HOMO to LUMO transition.[15] Taking the R6G molecule as an example, the adsorption and charge transfer between the R6G and $TaSe_2$ nanosheets was measured using Fourier transform infrared spectroscopy (FTIR) spectroscopy (Figure S7, Supporting Information), ultraviolet (UV)–vis spectroscopy (Figure S8, Supporting Information) and the fluorescence spectroscopy (Figure 4c). After mixing the R6G molecules with the $TaSe_2$ nanosheets, the R6G solution immediately turned from purple to red indicating the formation of an R6G-$TaSe_2$ complex. As shown in Figure 4b, the red R6G-$TaSe_2$ complex can be completely removed using centrifugation at 10 000 rpm to obtain a transparent supernatant (see the inset photograph in Figure 4b) and a brown sediment. The R6G-$TaSe_2$ complex, with an obvious absorption peak at 553 nm, decreases to a very small peak at 530 nm after centrifugation, demonstrating that most of the R6G molecules are adsorbed on the $TaSe_2$ nanosheets. The FTIR spectrum shown in Figure S7 in the Supporting Information reveals the $TaSe_2$ nanosheets do not exhibit obvious absorption. The R6G-$TaSe_2$ complex after centrifugation demonstrates the same FTIR absorption as that of the R6G molecules, indicating the highly efficient adsorption of R6G on $TaSe_2$ nanosheets. In Figure 4c, the electron transfer between the R6G molecules and the $TaSe_2$ nanosheets is confirmed as the photoluminescent peak of R6G at 552 nm, which is quenched upon addition of $TaSe_2$ nanosheets. Compared with MoS_2 and WS_2 (Figure S8, Supporting Information), the $TaSe_2$ nanosheets demonstrate the highest fluorescence quenching efficiency. The results from the DFT calculations are depicted in Figure 4d with the adsorption energies (E_{ads}) of the R6G molecule in parallel and perpendicular configurations on the 1T and 2H phase $TaSe_2$ layer. The parallel configurations possess the most stable state, exhibiting E_{ads} values of –1.93 and –2.17 eV for the 2H and 1T phases of $TaSe_2$, respectively. In contrast, E_{ads} values of –1.08 and –1.21 eV with perpendicular configurations are more positive than those observed for the parallel configurations suggesting a less stable state. The charge density difference of R6G molecules and $TaSe_2$ can be found in Figure S9 in the Supporting Information that more remarkable charge accumulation near the $TaSe_2$ and faster charge depletion near the R6G molecules occurs in the parallel configurations. The stronger electron transfer from the

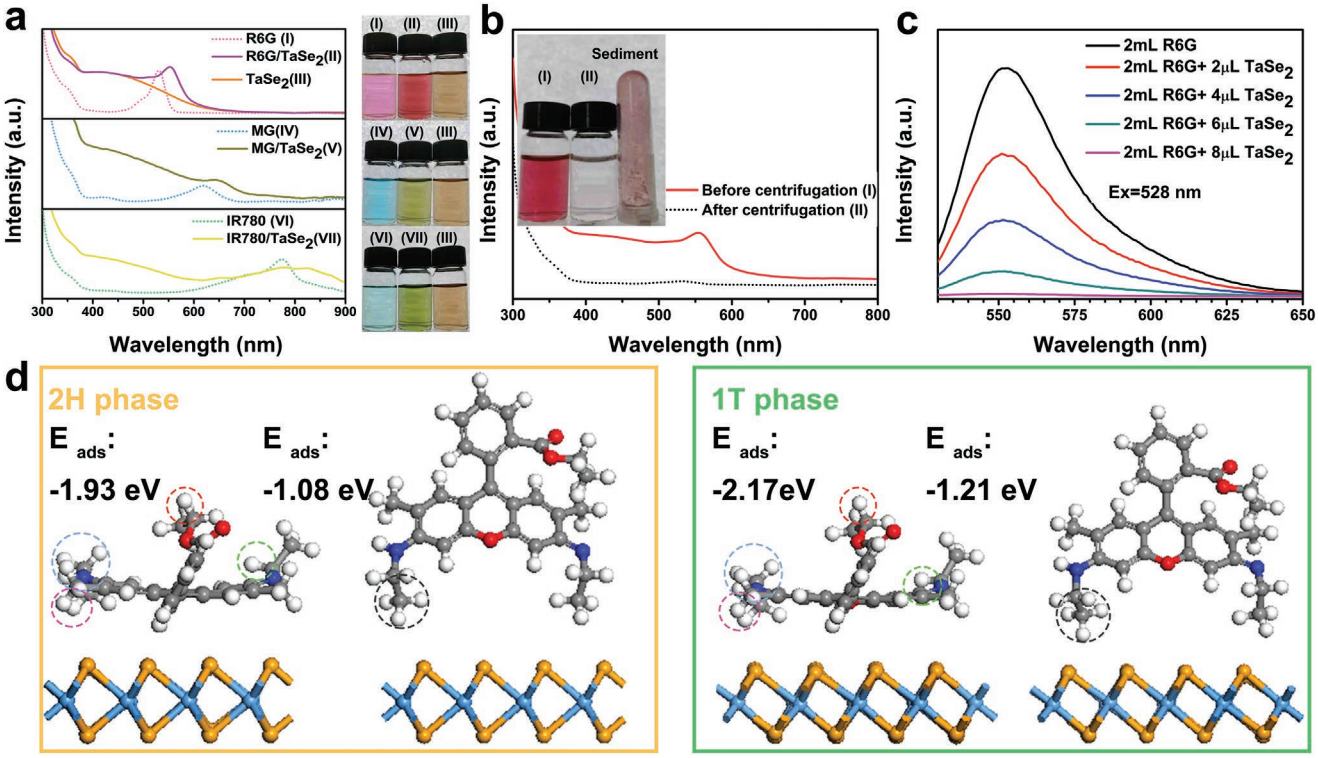

Figure 4. a,I) Absorption spectra for the pristine R6G solution, II) R6G solution mixed with $TaSe_2$ nanosheets, III) $TaSe_2$ nanosheets solution, IV) MG solution, V) MG solution mixed with $TaSe_2$ nanosheets, VI) IR780 solution, and VII) IR780 solution mixed with $TaSe_2$ nanosheets. The photograph shows the colors of the respective solutions. b) Absorption spectra of the R6G solution mixed with $TaSe_2$ nanosheets I) before and II) after centrifugation at 10 000 rpm for 3 min. The inset exhibits the color change of the R6G solution mixed with $TaSe_2$ and the supernatant after centrifugation. c) Photoluminescence spectra of the pristine R6G solution mixed with different amounts of the $TaSe_2$ nanosheets solution. d) DFT calculation results for the R6G molecules adsorbed on the 2H phase and 1T phase $TaSe_2$ with parallel and perpendicular configurations. The differences of parallel and vertical configurations of R6G molecule on 2H and 1T $TaSe_2$ are marked with circles.

R6G molecules to $TaSe_2$ are verified in the parallel configurations with both 2H and 1T phase $TaSe_2$. The same observation has been previously reported by Lv's group, who highlighted that the R6G molecules adsorbed on the graphene and the $NbSe_2$ layer are more stable in the parallel configurations.[21] The EM effect of the $TaSe_2$ nanosheets can be ruled out as no absorption peak shifts were observed in the absorption spectra of the nanosheets measured in solvents with different refractive indexes (Figure S10, Supporting Information).[54,55] The results also indicate that no obvious absorption of the surface plasmon resonance (SPR) can be detected at wavelengths ranging from 300 to 1000 nm. A previous study reported that the SPR of $TaSe_2$ mainly occurs in the terahertz and telecom range.[23]

The SERS mechanism can be described using a polarization tensor equation: $\alpha = A + B + C$, in which A denotes the molecular resonance and B and C represent the SPR and molecule-metal charge-transfer resonance at the Fermi level, respectively.[56] The SPR effect is excluded in this paper. Thus, only the other two resonances A and C are discussed. In addition to the static absorption and spectrum analysis of the R6G molecules on the surface of the $TaSe_2$ nanosheets, the PICT process of the CM is further depicted in **Figure 5**.[57,58] The HOMO and LUMO levels for the R6G molecules are −5.7 and −3.4 eV, respectively (the blue line).[19] As detailed in previous reports, the metallic properties of both the 2H and 1T phase $TaSe_2$ are verified in Figure 5a, and a significant amount of electrons can be observed across the Fermi levels.[38,59] The process of PICT comprises both the charge transfer from the R6G HOMO level to the $TaSe_2$ Fermi level and from the $TaSe_2$ Fermi level to the R6G LUMO level (Figure 5b), which is ascribed to the transfer of the conducting electron below the Fermi level of the metallic $TaSe_2$ to the CT transition.[19] This molecule-metal coupling can be described using the vibronic Herzberg–Teller theory, and the polarization tensor of the probe is largely magnified in this coupling system.[60] Moreover, the abundant electrons across the Fermi level of $TaSe_2$ can increase the number of allowed energy states for PICT with this molecule-metal coupling complex and it further increases the charge transition probability as depicted with Fermi's golden rule. The molecular fluorescence quenching shown in Figure 4c provides further direct evidence of the PICT process.[55] In addition to the PICT process, the molecular resonance is also important to the SERS performance[61] and the highest SERS signals only can be recorded at a specific laser wavelength of excitation (Figures 3d and 4a). Using the R6G molecules as an example, the HOMO–LUMO gap is about 2.3 eV, which can easily match the 532 nm wavelength (1240/532≈2.33 eV). The SERS signals decrease significantly if wavelengths of 633 and 785 nm are applied. Furthermore, it must also be established how $TaSe_2$ can outperform the most studied materials, MoS_2 and WS_2. The

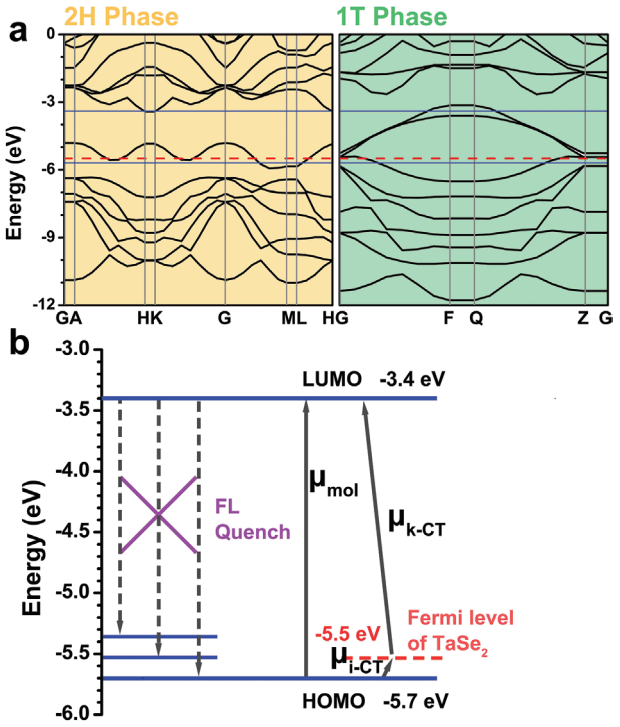

Figure 5. a) Band structures of the 2H and 1T phases of the $TaSe_2$ nanosheets. The red dashed lines denote the Fermi levels of the 2H and 1T $TaSe_2$ nanosheets and the blue solid lines denote the HOMO and LUMO of the R6G molecules. The Fermi levels are set at −5.5 eV according to the results of a previous study.[59] b) Diagram of the energy level and charge transfer in the R6G-$TaSe_2$ complex. μ_{mol} denotes the molecular transition. $\mu_{i\text{-}CT}$ and $\mu_{k\text{-}CT}$ denote the charge transfer from the HOMO of the R6G molecules to the $TaSe_2$ nanosheets and from the $TaSe_2$ nanosheets to the LUMO of the R6G molecules, respectively.

bandgaps of 0 eV are illustrated in Figure 5a for both the 2H and 1T phases of $TaSe_2$. Figures S11 and S12 in the Supporting Information demonstrate the bandgaps of the 2H phase MoS_2 and the WS_2 were observed to be 1.80 and 1.79 eV, respectively.[62,63] The 1T phase MoS_2 and WS_2 are metallic with a 0 eV bandgap, meaning that the 1T phase MoS_2 and WS_2, with an abundance of electrons filled close to the Fermi levels, can increase the SERS signals more efficiently through lithium intercalation and exfoliation. For $TaSe_2$, both the 1T and 2H phases are metallic and both can contribute to the SERS activity.

2.4. Detecting Bilirubin with $TaSe_2$

High levels of bilirubin can result in jaundice, which is a leading cause of neonatal death during the first day of life.[64] Furthermore, an increase in the normal concentration ($<25 \times 10^{-6}$ M) of bilirubin to a level that can result in jaundice ($>50 \times 10^{-6}$ M) can also potentially evoke mental disorders and permanent brain damage resulting from dysfunction of the hepatic or biliary tract.[65,66] A study previously published by Li's group demonstrates that graphene oxide and gold nanostars as SERS substrates can be employed for detection bilirubin molecules using a label-free SERS technique, as their large Raman scattering cross-section can produce strong SERS signals.[67] However, plasmon-free substrates such as the $TaSe_2$ film may provide as an economical and effective substrate for clinical diagnosis. The SERS signals at different laser wavelengths and the Raman spectrum of bilirubin are displayed in **Figure 6**a. The dominant Raman bands are listed in Table S1 in the Supporting Information, including the bands at 952 (out-of-plane CH vibration), 988 (CH_3 asymmetric deformation), 1190 ($C-CH_2$ bending), 1248 (CH wagging), 1268 (C−C stretching and N−H scissoring in lactam ring), 1290 (CH wagging), 1341 (C−CH bending in CH_3), 1363 (CH_2 scissoring), 1455 (C−C and C−N mixed stretching), 1500 (C=C stretching in ring and C−C stretching), 1572 (asymmetric C−N stretching in ring) and 1613 cm^{-1} (C=C stretching in the five-membered ring).[68,69] The strongest SERS signals of bilirubin on the $TaSe_2$ film are obtained for excitation using a laser at 532 nm. Notably, no SERS signal can be detected using a laser at 785 nm and only a weak response was observed at 633 nm (Figure 6a). Compared with 100×10^{-6} M of bilirubin on the $TaSe_2$ film, the bilirubin powder exhibits Raman signals that are sixfold lower (at 1611 cm^{-1}) with a 532 nm laser, indicating the significant SERS effect observed using the $TaSe_2$ film. The UV–vis spectrum is plotted in Figure 6b, and the absorption peak at 449 nm of bilirubin (molecular resonance) redshifts to 455 nm after being mixed with the $TaSe_2$ nanosheets, demonstrating the CM induced SERS mechanism.[61] Hence, a laser wavelength of 532 nm was selected as the optimum match for the molecular resonance of bilirubin and is used for the following SERS measurements. In ethanol, the intensity of the SERS signals declines significantly (Figure 6c), along with the decrement of the bilirubin concentration, denoting the proportion of the SERS intensity to the amount of bilirubin adsorbed on the $TaSe_2$ film surface. The SERS signals for the 1×10^{-6} M bilirubin solution are easily detected and signals representing the 0.316×10^{-6} M bilirubin solution at 988, 1341, and 1613 cm^{-1} readily can be observed. For the detection of bilirubin in serum, rabbit serum that does not contain detectable bilirubin was used in this study. The serum was centrifugated in a Millipore tube with centrifugal filters to eliminate the majority of the proteins and other large molecules. Figure 6d shows that the SERS signals of bilirubin in the serum are weaker than those observed in ethanol and the SERS signals of the bilirubin in serum gradually increase with the addition of bilirubin and an LOD as low as 0.316×10^{-6} M was obtained. This plasmon-free $TaSe_2$ film exhibits more than tenfold higher sensitivity than the noble metal (gold nanostars) based SERS sensor (5×10^{-6} M) on the detection of bilirubin.[67] Similar measurements were also performed in urine (Figure 6e), which shows a higher response than that exhibited in serum, but weaker than that observed in ethanol. The lower response can be ascribed to the nonspecific adsorption of other molecules from serum and urine on the $TaSe_2$ film, thus reducing the adsorption of bilirubin and resulting in a lower SERS intensity for the bilirubin. However, the Raman signal of bilirubin can still be detected, indicating the small Raman cross-sections and/or the low concentration of the other interferent molecules. The results indicate that the $TaSe_2$ film provides a high sensitivity and Raman enhancement for the detection of bilirubin in these complex media. The intensity of the SERS signals at 1611 cm^{-1} shows the linear correlation with the logarithmic concentration

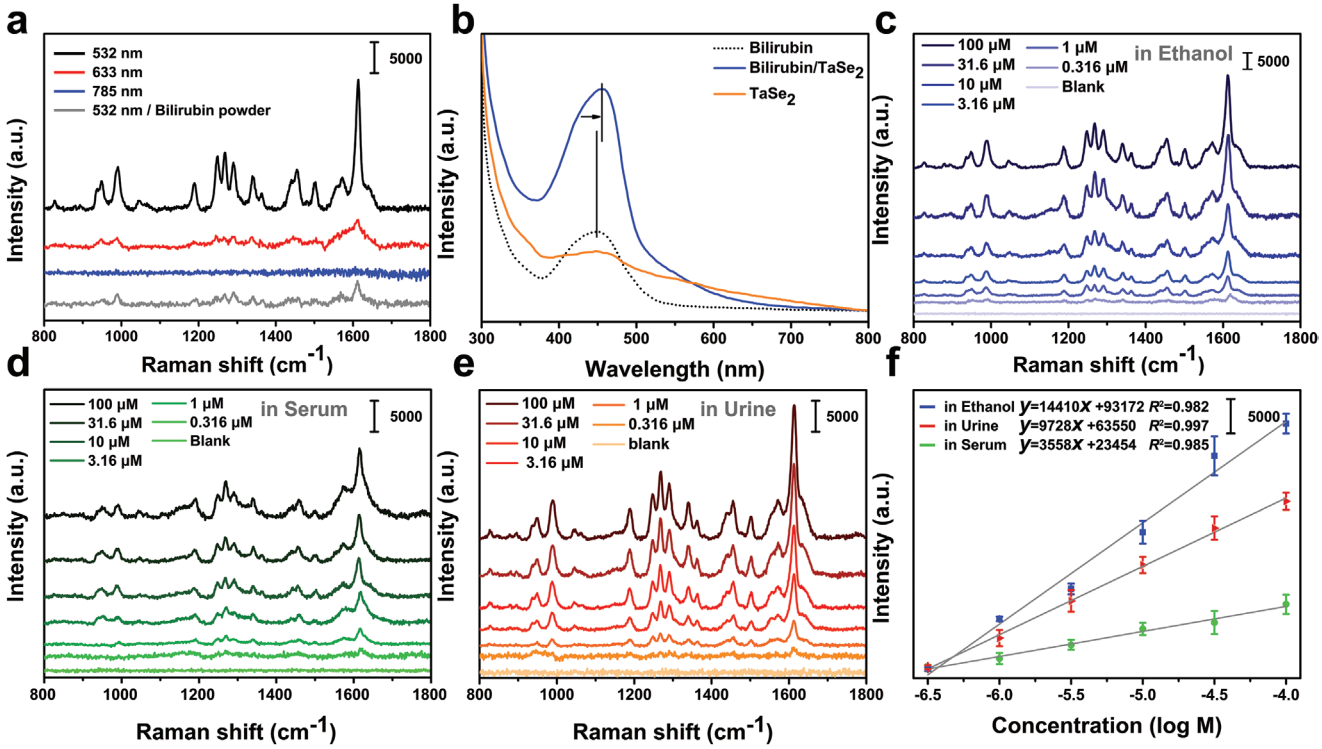

Figure 6. a) SERS spectra of 100×10^{-6} M bilirubin incubated on the $TaSe_2$ film measured at different wavelengths and the Raman spectra of bilirubin powder measured using a 532 nm wavelength laser. b) Absorption spectra of the pristine bilirubin solution (black dashed line), bilirubin solution mixed with $TaSe_2$ nanosheets (blue line), and $TaSe_2$ nanosheets (orange line). SERS spectra of bilirubin with various concentrations of bilirubin ranging from 100×10^{-6} to 0.316×10^{-6} M in c) ethanol, d) serum, and e) urine. Note that the Raman signal for 0.316×10^{-6} M bilirubin and the blank samples have been multiplied by three to provide a clear illustration. f) Linear plots of the SERS intensities at a Raman shift of 1611 cm^{-1} versus the logarithm of the bilirubin concentration.

(0.316×10^{-6}–100×10^{-6} M) of bilirubin (Figure 6f). The small variations obtained from the measurement of three different $TaSe_2$ films and the excellent linear relationship observed in ethanol, serum, and urine demonstrate the high reproducibility, reliability, and potential of the $TaSe_2$ film for quantitative analysis of bilirubin. This material and the methods reported in this study indicate the feasibility of further applications in the diagnosis of jaundice by extensive analysis of clinical samples.

3. Conclusion

A convenient method was used to fabricate an atomically thin $TaSe_2$ film that demonstrates excellent sensitivity, reproducibility, and reliability for SERS analysis. Systematic experiments and DFT calculations were used to demonstrate high SERS performance of the $TaSe_2$ film derived from the CM effect instead of the SPR effect. The metallic properties in both the 2H and 1T phases of the $TaSe_2$ nanosheets significantly increased the charge transition probability from the HOMO level to the LUMO level of the adsorbed probe molecules through the PICT process. In addition, the molecular resonance is also essential for SERS measurements if combined with a well-matched laser wavelength. The SERS performance of the $TaSe_2$ film cannot outperform state-of-the-art materials such as CVD prepared NbS_2 and $NbSe_2$.[15,21] However, it exhibits a more economical method for the fabrication of large scale 2D films for the detection of bilirubin, the biomarker for jaundice (which is considered as the dominant cause of death in newborns), in serum and urine. Taken together, the atomically thin $TaSe_2$ film offers an attractive avenue for applications in plasmon-free SERS detection of target of relevance in clinical diagnostics. We believe more research works may be inspired by exploring other semimetallic 2D materials with abundant charge carrier density and their CM effect should not be underestimated.

4. Experimental Section

Chemical Reagent: $TaSe_2$ powder was purchased from Nanjing MKnano Tech and has a particle size of 5–20 μm. R6G, MG, IR780, bilirubin, *n*-butyllithium (2.5 M in *n*-hexane), anhydrous *n*-hexane, polyvinyl pyrrolidone, and anhydrous ethanol were purchased from Shanghai Macklin Biochemical Co., Ltd and used without further purification. Normal rabbit serum was purchased from Wuhan AmyJet Scientific Inc.

Chemical Exfoliation: $TaSe_2$ powder was dried in a vacuum oven at 85 °C for 12 h prior to use. The intercalation of lithium ions into the $TaSe_2$ powder was performed according to a previously reported method to exfoliate the MoS_2.[70] Briefly, 200 mg $TaSe_2$ was mixed with 2.5 mL *n*-butyllithium in 10 mL *n*-hexane and stirred at 55 °C for 3 d under an inert atmosphere. The obtained precipitate was quenched with deionized water and washed with ethanol several times. The precipitate was then sonicated in 35 mL degassed water for 1 h and centrifugated

at 1000 rpm for 10 min to remove the nonexfoliated materials, 30 mL of the brown supernatant was obtained and was frozen using liquid nitrogen and stored at −20 °C. The concentration of the $TaSe_2$ dispersion was calculated to be ≈3 mg mL^{-1} by weighing 20 mL of the freeze-dried sample.

Constructing the SERS Substrate: The atomically thin $TaSe_2$ film on AAO substrate was prepared by dispersing 100 µL of the $TaSe_2$ nanosheets in 10 mL ethanol to form a homogeneous solution. The diluted $TaSe_2$ solution was filtered through an AAO substrate with a diameter of 2.5 cm and a pore size of 90 nm. Then, the $TaSe_2$ film supported on AAO was dried in a vacuum oven at 40 °C for 1 h. The thickness of the $TaSe_2$ film was calculated and details are provided in Figure S3 in the Supporting Information.

SERS Measurements: The AAO substrate covered with $TaSe_2$ film was cut to a size of 5 × 5 mm and immersed in 100 µL of the SERS probes at different concentrations dispersed in ethanol. After 15 min, the $TaSe_2$ film was washed with ethanol three times and dried in an ambient environment. For serum spiked with bilirubin, 100 µL serum was added to a 0.5 mL Millipore tube (Amicon Ultra-4 3KD) with cellulose filters and centrifugated at 10 000 rpm for 20 min. Then, the $TaSe_2$ film was soaked in ≈100 µL of the serum for 15 min, washed with ethanol three times, and dried in an ambient environment. The spiked urine samples were used directly without extra processing. Every sample was tested using three different $TaSe_2$ films with ten sites to determine the SERS intensity.

The SERS measurements were performed using a microscopic confocal Raman spectrometer (Renishaw inVia). A laser power of 5 mW, an exposure time of 0.1 s and an accumulation number of 30 times using an L50 objective lens were utilized for all SERS measurements. To test different SERS probes, laser wavelengths of 532, 633, and 785 nm were used.

The values of EF were calculated using the following equation[22]

$$EF = \frac{I_{SERS}}{C_{SERS}} / \frac{I_{Raman}}{C_{Raman}} \quad (1)$$

In which I_{SERS} and I_{Raman} refer to the intensity of the probe molecules in the SERS and Raman spectra and C_{SERS} and C_{Raman} denote the concentration of the probe molecules in the SERS and Raman spectra. Table S3 in the Supporting Information shows the EF of $TaSe_2$, MoS_2, and WS_2.

Characterization: Morphology and structural tests were performed using SEM, TEM, and AFM. The SEM samples were prepared by drop-casting 1.5 µL of the $TaSe_2$ dispersion onto the AAO membranes (at a hole size of 90 nm and a hole depth of 200 µm) and dried at 40 °C in a vacuum oven. The SEM measurements were carried out using a HITACHI SU8010 at an accelerating voltage of 1.5 kV. The TEM samples were prepared by dispersing 5 µL $TaSe_2$ solution in 100 µL ethanol, then a copper grid with an ultrathin carbon film (Beijing Zhongjingkeyi Technology Co., Ltd.) was soaked in the solution for 2 min. The copper grid was then dried at 40 °C in a vacuum oven. FEI Talos F200S with an accelerating voltage of 200 kV was used to record the high-resolution TEM images and the energy dispersive X-ray spectroscopy mapping images. The AFM tests were performed using a Bruker Dimension Icon equipment.

The UV–vis absorption spectra were performed using an Agilent CARY5000, the FTIR measurements were carried out using a Bruker Tensor II, and the fluorescence spectra were obtained on a Horiba FluoroMax-4. XPS analysis was performed on a Perkin-Elmer PHI 5000C electron spectroscopy for chemical analysis (ESCA) using a Mg anode as the excitation source. The PXRD spectra were obtained using a Bruker R8 Advance instrument.

DFT Calculations: The Cambridge Sequential Total Energy Package embedded in Material Studio was utilized to perform the DFT calculations and analysis.[71] The Perdew–Burke–Ernzerhof generalized gradient approximation functional was used in all simulations and the DFT-D1 method was utilized to describe the van der Waals forces.[72,73] For band structure calculations, unit cells of the TMDs (MoS_2, WS_2, and $TaSe_2$) with both 1T and 2H phases were considered with a vacuum layer of 15 Å. To calculate the adsorption energy of the R6G molecules, a 4 × 4 supercell of one-layer of $TaSe_2$ with a vacuum layer of 20 Å was built. A R6G molecule with parallel and vertical structures on the surface of $TaSe_2$ was optimized. The parameters were a cutoff energy of 500 eV, an energy convergence of 10^{-6} eV and a residual force convergence of 0.001 eV $Å^{-1}$. The Monkhorst–Pack grid *k*-points of 10 × 10 × 2 and 3 × 3 × 2 were set for calculations of the electronic structure and adsorption, respectively. The adsorption energy (E_{ad}) can be determined as $E_{ad} = E_{total} - E_{slab} - E_{mol}$, in which E_{total}, E_{slab}, and E_{mol} are the energies of the adsorbed molecule on the slab, isolated slab, and isolated molecular, respectively.

Supporting Information

Supporting Information is available from the Wiley Online Library or from the author.

Acknowledgements

Y.G. and F.W. contributed equally to this work. This work was financially supported by Zhejiang Province Natural Science Fund for Distinguished Young Scholars (Grant No. LR19H180001), Science and Technology Development Project of Wenzhou Longwan's (2016YG15), Leading Talent Innovation and Entrepreneurship Project of Wenzhou (RX2016005), and Publica Projects of Wenzhou (2020005). The authors would like to thank the Analytical & Testing Center of Sichuan University for providing simulation tools.

Conflict of Interest

The authors declare no conflict of interest.

Data Availability Statement

The data that support the findings of this study are available from the corresponding author upon reasonable request.

Keywords

2D materials, clinical diagnosis, surface-enhanced Raman spectroscopy, $TaSe_2$

Received: November 14, 2021
Revised: February 8, 2022
Published online:

[1] J. Langer, D. Jimenez de Aberasturi, J. Aizpurua, R. A. Alvarez-Puebla, B. Auguie, J. J. Baumberg, G. C. Bazan, S. E. J. Bell, A. Boisen, A. G. Brolo, J. Choo, D. Cialla-May, V. Deckert, L. Fabris, K. Faulds, F. J. Garcia de Abajo, R. Goodacre, D. Graham, A. J. Haes, C. L. Haynes, C. Huck, T. Itoh, M. Kall, J. Kneipp, N. A. Kotov, H. Kuang, E. C. Le Ru, H. K. Lee, J.-F. Li, X. Y. Ling, et al., *ACS Nano* **2019**, *14*, 28.
[2] L. Zhang, M. Fang, *Nano Today* **2010**, *5*, 128.
[3] S. Laing, L. E. Jamieson, K. Faulds, D. Graham, *Nat. Rev. Chem.* **2017**, *1*, 0060.
[4] M. Fleischmann, P. J. Hendra, A. J. McQuillan, *Chem. Phys. Lett.* **1974**, *26*, 163.
[5] G. Wang, C. Hao, W. Ma, A. Qu, C. Chen, J. Xu, C. Xu, H. Kuang, L. Xu, *Adv. Mater.* **2021**, *33*, 2102337.

[6] S. Luo, A. Mancini, R. Berte, B. H. Hoff, S. A. Maier, J. C. de Mello, *Adv. Mater.* **2021**, *33*, 2100491.
[7] S. Y. Ding, E. M. You, Z. Q. Tian, M. Moskovits, *Chem. Soc. Rev.* **2017**, *46*, 4042.
[8] L. Yang, P. Li, H. Liu, X. Tang, J. Liu, *Chem. Soc. Rev.* **2015**, *44*, 2837.
[9] E. C. Le Ru, P. G. Etchegoin, *Annu. Rev. Phys. Chem.* **2012**, *63*, 65.
[10] X. X. Han, W. Ji, B. Zhao, Y. Ozaki, *Nanoscale* **2017**, *9*, 4847.
[11] I. Alessandri, J. R. Lombardi, *Chem. Rev.* **2016**, *116*, 14921.
[12] S. A. Ghopry, M. A. Alamri, R. Goul, R. Sakidja, J. Z. Wu, *Adv. Opt. Mater.* **2019**, *7*, 1801249.
[13] M. Li, Y. Gao, X. Fan, Y. Wei, Q. Hao, T. Qiu, *Nanoscale Horiz.* **2021**, *6*, 186.
[14] X. Ling, J. Wu, L. Xie, J. Zhang, *J. Phys. Chem. C* **2013**, *117*, 2369.
[15] X. Song, Y. Wang, F. Zhao, Q. Li, T. Huy Quang, M. H. Ruemmeli, C. G. Tully, Z. Li, W.-J. Yin, L. Yang, K.-B. Lee, J. Yang, I. Bozkurt, S. Liu, W. Zhang, M. Chhowalla, *ACS Nano* **2019**, *13*, 8312.
[16] S. M. Feng, M. C. dos Santos, B. R. Carvalho, R. T. Lv, Q. Li, K. Fujisawa, A. L. Elias, Y. Lei, N. Perea-Lopez, M. Endo, M. H. Pan, M. A. Pimenta, M. Terrones, *Sci. Adv.* **2016**, *2*, 12.
[17] Y. Yin, P. Miao, Y. Zhang, J. Han, X. Zhang, Y. Gong, L. Gu, C. Xu, T. Yao, P. Xu, Y. Wang, B. Song, S. Jin, *Adv. Funct. Mater.* **2017**, *27*, 1606694.
[18] Y. Liu, Z. Gao, M. Chen, Y. Tan, F. Chen, *Adv. Funct. Mater.* **2018**, *28*, 1805710.
[19] L. Tao, K. Chen, Z. Chen, C. Cong, C. Qiu, J. Chen, X. Wang, H. Chen, T. Yu, W. Xie, S. Deng, J. B. Xu, *J. Am. Chem. Soc.* **2018**, *140*, 8696.
[20] B. Soundiraraju, B. K. George, *ACS Nano* **2017**, *11*, 8892.
[21] Q. Lv, X. Wu, J. Tan, B. Liu, L. Gan, J. Li, Z.-H. Huang, F. Kang, R. Lv, *J. Mater. Chem. A* **2021**, *9*, 2725.
[22] K. Wang, Z. Guo, Y. Li, Y. Guo, H. Liu, W. Zhang, Z. Zou, Y. Zhang, Z. Liu, *ACS Appl. Nano Mater.* **2020**, *3*, 11363.
[23] C. Song, X. Yuan, C. Huang, S. Huang, Q. Xing, C. Wang, C. Zhang, Y. Xie, Y. Lei, F. Wang, L. Mu, J. Zhang, F. Xiu, H. Yan, *Nat. Commun.* **2021**, *12*, 386.
[24] C. S. Lian, C. Heil, X. Liu, C. Si, F. Giustino, W. Duan, *J. Phys. Chem. Lett.* **2019**, *10*, 4076.
[25] Y. Chen, W. Ruan, M. Wu, S. Tang, H. Ryu, H.-Z. Tsai, R. L. Lee, S. Kahn, F. Liou, C. Jia, O. R. Albertini, H. Xiong, T. Jia, Z. Liu, J. A. Sobota, A. Y. Liu, J. E. Moore, Z.-X. Shen, S. G. Louie, S.-K. Mo, M. F. Crommie, *Nat. Phys.* **2020**, *16*, 218.
[26] E. Er, H.-L. Hou, A. Criado, J. Langer, M. Möller, N. Erk, L. M. Liz-Marzán, M. Prato, *Chem. Mater.* **2019**, *31*, 5725.
[27] S. Parida, A. Mishra, J. Chen, J. Wang, A. Dobley, C. B. Carter, A. M. Dongare, *J. Am. Ceram. Soc.* **2020**, *103*, 6603.
[28] L. Wang, Z. Xu, W. Wang, X. Bai, *J. Am. Ceram. Soc.* **2014**, *136*, 6693.
[29] C. Lin, X. Zhu, J. Feng, C. Wu, S. Hu, J. Peng, Y. Guo, L. Peng, J. Zhao, J. Huang, J. Yang, Y. Xie, *J. Am. Chem. Soc.* **2013**, *135*, 5144.
[30] H. Wang, Y. Chen, C. Zhu, X. Wang, H. Zhang, S. H. Tsang, H. Li, J. Lin, T. Yu, Z. Liu, E. H. T. Teo, *Adv. Funct. Mater.* **2020**, *30*, 2001903.
[31] S. Chowdhury, H. M. Hill, A. F. Rigosi, A. Briggs, H. Berger, D. B. Newell, A. R. Hight Walker, F. Tavazza, *ACS Appl. Nano Mater.* **2021**, *4*, 1810.
[32] J. A. Holy, M. V. Klein, W. L. McMillan, S. F. Meyer, *Phys. Rev. Lett.* **1976**, *37*, 1145.
[33] J. C. Tsang, M. W. Shafer, *Solid State Commun.* **1978**, *25*, 999.
[34] A. Molina-Sánchez, L. Wirtz, *Phys. Rev. B* **2011**, *84*, 155413.
[35] Y. Xu, K. Wang, Z. Yao, J. Kang, D. Lam, D. Yang, W. Ai, C. Wolverton, M. C. Hersam, Y. Huang, W. Huang, V. P. Dravid, J. Wu, *Small* **2021**, *17*, 2100637.
[36] S. Gong, G. Zhao, P. Lyu, K. Sun, *Small* **2018**, *14*, 1803344.
[37] X. Ji, D. Ding, X. Guan, C. Wu, H. Qian, J. Cao, J. Li, C. Jin, *ACS Nano* **2021**, *15*, 15039.
[38] Q. H. Wang, K. Kalantar-Zadeh, A. Kis, J. N. Coleman, M. S. Strano, *Nat. Nanotechnol.* **2012**, *7*, 699.
[39] M. Kamaratos, C. A. Papageorgopoulos, D. C. Papageorgopoulos, D. Tonti, C. Pettenkofer, W. Jaegermann, *Appl. Surf. Sci.* **1999**, *147*, 101.
[40] H. J. Crawack, C. Pettenkofer, *Solid State Commun.* **2001**, *118*, 325.
[41] S. Nie, S. R. Emory, *Science* **1997**, *275*, 1102.
[42] G. Upender, R. Satyavathi, B. Raju, K. Shadak Alee, D. Narayana Rao, C. Bansal, *Chem. Phys. Lett.* **2011**, *511*, 309.
[43] X. Zhang, X. Zhang, C. Luo, Z. Liu, Y. Chen, S. Dong, C. Jiang, S. Yang, F. Wang, X. Xiao, *Small* **2019**, *15*, 1805516.
[44] J. Zhou, P. L. Zhou, Q. Shen, S. A. Ahmed, X. T. Pan, H. L. Liu, X. L. Ding, J. Li, K. Wang, X. H. Xia, *Anal. Chem.* **2021**, *93*, 11679.
[45] J. Chen, Y. Wu, C. Fu, H. Cao, X. Tan, W. Shi, Z. Wu, *Biosens. Bioelectron.* **2019**, *143*, 111619.
[46] G.-N. Xiao, S.-Q. Man, *Spectrosc. Lett.* **2013**, *46*, 577.
[47] Y. Zhang, W. Yu, L. Pei, K. Lai, B. A. Rasco, Y. Huang, *Food Chem.* **2015**, *169*, 80.
[48] H. Wu, Y. Song, G. Yu, X. Chen, Y. Yang, *J. Raman Spectrosc.* **2016**, *47*, 1213.
[49] M. Potara, T. Nagy-Simon, M. Focsan, E. Licarete, O. Soritau, A. Vulpoi, S. Astilean, *Colloids Surf., B* **2021**, *203*, 111755.
[50] X. Huang, Y. Yin, M. Wu, W. Zan, Q. Yang, *Chin. Chem. Lett.* **2019**, *30*, 1335.
[51] A. Castellanos-Gomez, E. Navarro-Moratalla, G. Mokry, J. Quereda, E. Pinilla-Cienfuegos, N. Agraït, H. S. J. van der Zant, E. Coronado, G. A. Steele, G. Rubio-Bollinger, *Nano Res.* **2013**, *6*, 191.
[52] Z. Zhu, Y. Zou, W. Hu, Y. Li, Y. Gu, B. Cao, N. Guo, L. Wang, J. Song, S. Zhang, H. Gu, H. Zeng, *Adv. Funct. Mater.* **2016**, *26*, 1793.
[53] Y. Peng, C. Lin, L. Long, T. Masaki, M. Tang, L. Yang, J. Liu, Z. Huang, Z. Li, X. Luo, J. R. Lombardi, Y. Yang, *Nano-Micro Lett.* **2021**, *13*, 52.
[54] R. A. Karaballi, G. Humagain, B. R. A. Fleischman, M. Dasog, *Angew. Chem., Int. Ed. Engl.* **2019**, *58*, 3147.
[55] G. Song, W. Gong, S. Cong, Z. Zhao, *Angew. Chem., Int. Ed. Engl.* **2021**, *60*, 5505.
[56] J. R. Lombardi, R. L. Birke, *J. Phys. Chem. C* **2008**, *112*, 5605.
[57] C. Muehlethaler, C. R. Considine, V. Menon, W.-C. Lin, Y.-H. Lee, J. R. Lombardi, *ACS Photonics* **2016**, *3*, 1164.
[58] X. Wang, W. Shi, S. Wang, H. Zhao, J. Lin, Z. Yang, M. Chen, L. Guo, *J. Am. Ceram. Soc.* **2019**, *141*, 5856.
[59] D. Tsoutsou, K. E. Aretouli, P. Tsipas, J. Marquez-Velasco, E. Xenogiannopoulou, N. Kelaidis, S. Aminalragia Giamini, A. Dimoulas, *ACS Appl. Mater. Interfaces* **2016**, *8*, 1836.
[60] J. R. Lombardi, R. L. Birke, *J. Chem. Phys.* **2012**, *136*, 144704.
[61] M. J. Walte, N. J. Borys, G. Gaefke, S. Höger, J. M. Lupton, *J. Am. Chem. Soc.* **2008**, *130*, 16830.
[62] B. G. Shin, G. H. Han, S. J. Yun, H. M. Oh, J. J. Bae, Y. J. Song, C. Y. Park, Y. H. Lee, *Adv. Mater.* **2016**, *28*, 9378.
[63] W. Zhao, R. M. Ribeiro, M. Toh, A. Carvalho, C. Kloc, A. H. Castro Neto, G. Eda, *Nano Lett.* **2013**, *13*, 5627.
[64] B. O. Olusanya, M. Kaplan, T. W. R. Hansen, *Lancet Child Adolesc.* **2018**, *2*, 610.
[65] V. Hooda, A. Gahlaut, A. Gothwal, V. Hooda, *Biotechnol. Lett.* **2017**, *39*, 1453.
[66] V. Subbiah, H. J. West, *JAMA Oncol.* **2016**, *2*, 1103.
[67] X. Pan, L. Li, H. Lin, J. Tan, H. Wang, M. Liao, C. Chen, B. Shan, Y. Chen, M. Li, *Biosens. Bioelectron.* **2019**, *145*, 111713.
[68] F. Celis, M. M. Campos-Vallette, J. S. Gómez-Jeria, R. E. Clavijo, G. P. Jara, C. Garrido, *Spectrosc. Lett.* **2016**, *49*, 336.
[69] A. K. Rai, S. B. Rai, D. K. Rai, V. B. Singh, *Spectrochim. Acta A* **2002**, *58*, 2145.
[70] I. Janica, D. Iglesias, S. Ippolito, A. Ciesielski, P. Samori, *Chem. Commun.* **2020**, *56*, 15573.
[71] S. J. Clark, M. D. Segall, C. J. Pickard, P. J. Hasnip, M. I. J. Probert, K. Refson, M. C. Payne, *Z. Kristallogr. Cryst. Mater.* **2005**, *220*, 567.
[72] J. P. Perdew, K. Burke, M. Ernzerhof, *Phys. Rev. Lett.* **1996**, *77*, 3865.
[73] J. Klimes, A. Michaelides, *J. Chem. Phys.* **2012**, *137*, 120901.